Microporous and Mesoporous Materials 344 (2022) 112207

Contents lists available at ScienceDirect

Microporous and Mesoporous Materials

journal homepage: www.elsevier.com/locate/micromeso

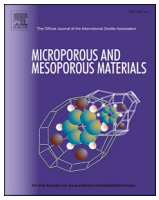

HNTs@HKUST-1 strengthened PAAm hydrogel for strain sensing and antibacterial application

Wanli Zhao, Yuanhui Long, Yunqing He, Jiabing Cai, Mingxian Liu *

Department of Materials Science and Engineering, College of Chemistry and Materials Science, Jinan University, Guangzhou, 511443, People's Republic of China

ARTICLE INFO

Keywords:
Halloysite nanotubes
Metal-organic framework
Hydrogel
Antibacterial properties
Sensing

ABSTRACT

Highly stretchable hydrogel shows great potential for wearable strain sensors. However, the rapid propagation of bacteria while using wearable sensors may threaten health. In this work, HNTs@HKUST-1 composites were prepared by the incorporation of halloysite nanotubes (HNTs) during the synthesis of HKUST-1. HNTs depressed the crystal growth of the HKUST-1, which leads to the 2D nanosheet morphology. HNTs@HKUST-1 serves as a reinforcing agent for polyacrylamide (PAAm) hydrogels, and PAAm-HNTs@HKUST-1 has high tensile strain properties (elongation at break of 912.5% and tensile strength of 22.4 kPa). The Cu^{2+} in HKUST-1 endows remarkable conductivity and excellent antibacterial properties to the composite. The composite hydrogels were then developed as human motion detection sensors with antibacterial property to prevent microbial infection, which show recyclability, high sensitivity, and fast responsiveness. So, they have great potential as flexible antibacterial materials to monitor movements of the human body in real-time.

1. Introduction

With the rapid development of artificial intelligence and electronic information technology, flexible wearable devices show a bright prospect [1]. Sensors are core components of flexible electronic devices, so sensors with intrinsic flexibility, high sensitivity, and real-time responsiveness are desired [2]. Flexible strain sensors have been developed for applications in human motion detection [3], human-computer interaction systems [4], electronic skin [5], and personalized medical diagnosis [6]. However, the design and fabrication of materials with high electrical conductivity, high flexibility, stretchability, and durability still lack critical technologies [2,7,8].

Hydrogels are three-dimensional network structures with excellent mechanical properties and tissue compatibility. It composes of hydrophilic polymers by physical or chemical cross-linking [9], in which a large amount of water can be preserved, which makes it widely used in many fields [10,11]. The works on the development of flexible strain sensors based on conductive hydrogels have been carried out extensively [12,13], and hydrogels are easily modified to obtain high flexibility, adhesion, strain sensitivity, and electrical conductivity. For example, Liu et al. prepared high-strength conductive hydrogels with both self-healing and self-adhesive properties, which were applied to monitor real-time human movement changes [14]. Wei et al. obtained freeze-resistant, highly sensitive, and long-term environmentally stable conductive hydrogels by introducing highly conductive MXene nanosheets into a tannic acid-modified cellulose nanofiber/polyacrylamide gel network [15]. However, conductive hydrogels also have some problems and drawbacks. The high content of water provides a suitable environment for microorganisms to thrive, which can lead to wound infection when used for human sensing. Therefore, it will be a challenging task to develop conductive hydrogel with a combination of excellent mechanical properties, high electrical conductivity, and antibacterial properties for applications in human motion sensors.

Polyacrylamide (PAAm) hydrogels are easy to prepare without complex instruments, which makes them suitable for the construction of multifunctional conductive hydrogels [16–18]. The mechanical strength of pure PAAm hydrogel is poor and difficult to withstand large strains, so it cannot meet the application requirements of flexible electronic devices. An effective approach to solve this problem is to introduce nanomaterials into the PAAm hydrogel network to enhance the mechanical properties of the hydrogel. Clay possesses unique structure and properties, which are commonly used for reinforcing hydrogel materials [19–21]. Among them, halloysite nanotubes (HNTs) with a formula of $Al_2Si_2O_5(OH)_4$ represented a novel tubular clay material for preparing high-performance and functional hydrogel [22]. HNTs typically show length in 200-1000 nm, while the inner and outer diameters are 15–30

* Corresponding author.
E-mail address: liumx@jnu.edu.cn (M. Liu).

https://doi.org/10.1016/j.micromeso.2022.112207
Received 7 June 2022; Received in revised form 28 August 2022; Accepted 29 August 2022
Available online 7 September 2022

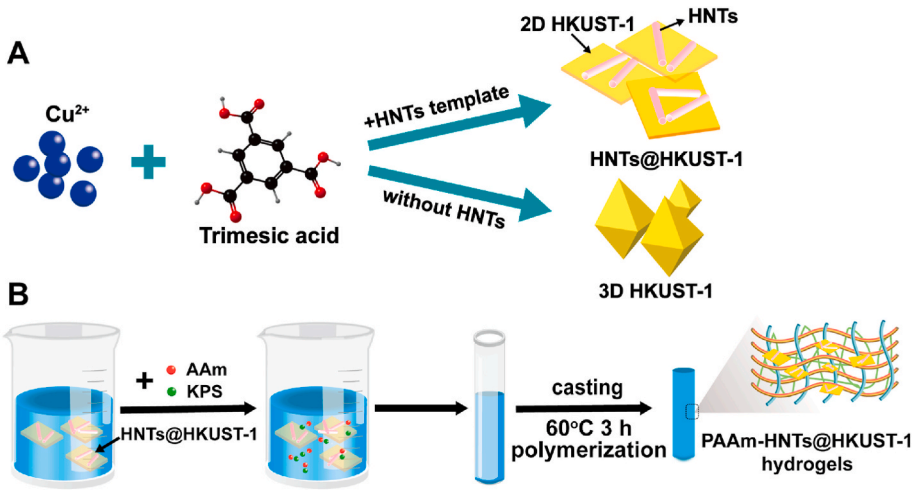

Fig. 1. (A) Schematic diagram of the synthesis of HNTs@HKUST-1 and HKUST-1. (B) Schematic illustration of the preparation process of PAAm-HNTs@HKUST-1 hydrogels.

nm, and 50–70 nm, respectively [23,24]. HNTs are a good candidate for the preparation of composite hydrogels due to their high aspect ratio, good dispersibility, good biocompatibility, and high surface reactivity. [25–27]. For example, Feng et al. introduced HNTs as a physical cross-linking agent into the PAAm hydrogel network and then soaked them in ethanol to make the cross-linked network tighter. The mechanical properties of the resulting composite hydrogels were substantially improved [28]. Other nanoparticles such as laponite, carbon nanotubes, and graphene could also be used to reinforce the PAAm hydrogel's mechanical properties for multi-functional applications [29].

HKUST-1 is a copper-based metal-organic framework (MOF) that can be used as an antimicrobial agent in hydrogels, exhibiting high electrical conductivity due to the presence of copper ions. In this work, sheet-like HKUST-1 were synthesized from a water/ethanol system by incorporating HNTs. The structure and antibacterial properties of the HNTs@HKUST-1 were investigated. Then, a conductive PAAm hydrogel was prepared by adding HNTs@HKUST-1 during the *in-situ* polymerization of acrylamide. The prepared PAAm-HNTs@HKUST-1 hydrogel achieved high electrical conductivity, excellent tensile strain, and excellent antibacterial properties. Compared to the PAAm-HNTs hydrogel, the tensile strain increased from 359.3% to 912.5%, which proves that it can be applied to detect large-amplitude movements, such as knee and elbow bending. The hydrogel shows good electrical conductivity and high sensor sensitivity. Besides, PAAm-HNTs@HKUST-1 hydrogel has excellent antibacterial properties against *E. coli* and *S. aureus*. The PAAm-HNTs@HKUST-1 composite hydrogels have great potential as flexible antibacterial materials to monitor the movements of the human body in real time.

2. Experimental section

2.1. Materials

Halloysite nanotubes (HNTs) were purchased from Guangzhou Runwo Materials Technology Co., Ltd., China. Cupric nitrate trihydrate ($Cu(NO_3)_2{\cdot}3H_2O$) and trimesic acid were provided by Shanghai Macklin Biochemical Technology Co., Ltd., China. Sodium bicarbonate ($NaHCO_3$) was bought from Shanghai Aladdin Biochemical Technology Co., Ltd., China. Acrylamide (AM, C_3H_5NO) was supplied by Aladdin Biochemical Technology Co., Ltd., China. Potassium persulfate (KPS, $K_2S_2O_8$) was bought from Tianjin Baishi Chemical Co., Ltd., China. Anhydrous ethanol was supplied by Tianjin Fuyu Fine Chemical Co., Ltd., China.

2.2. Preparation of HKUST-1 and HNTs@HKUST-1 nanocomposites

The preparation of HNTs@HKUST-1 was performed according to a previous study with slight modification [30]. The synthesis process of HKUST-1 and HNTs@HKUST-1 is shown in Fig. 1A. The typical procedure was as below. HNTs (0.35 g, 1.4 mmol) were uniformly dispersed in 10 mL of ethanol and sonicated for 30 min. $Cu(NO_3)_2{\cdot}3H_2O$ (0.86 g, 3.57 mmol) was dissolved in 40 mL of ethanol. Then, they were mixed and sonicated for 30 min. After that, 0.5 g (2.38 mmol) trimesic acid and 0.6 g (7.14 mmol) $NaHCO_3$ (1:3) were dissolved in 150 mL of deionized water and added to the mixture. The mixture was stirred for 16 h at room temperature. Finally, the product was collected by centrifugation, washed 3 times with ethanol and water, and dried in an oven at 60 °C. HKUST-1 was prepared similarly as above without the addition of HNTs.

2.3. Preparation of PAAm-HNTs@HKUST-1 composite hydrogels

The preparation process of PAAm-HNTs@HKUST-1 composites is shown in Fig. 1B. Four sets of solutions were prepared by adding 0.4 g HNTs, 0.1 g, 0.2 g, and 0.4 g HNTs@HKUST-1 in 20 mL of water and sonicated for 30 min to make them well dispersed. Next, 3 g of AM was added to each of the solutions and stirred for 30 min at room temperature. Then, 0.6 g of KPS was dissolved in 3 mL of water and added to each of the solutions with stirring for 10 min. After that, each group of solutions was poured into test tubes (1 cm in diameter and 10 cm in length) and reacted in an oven at 60 °C for 3 h. After the reaction, the hydrogels were obtained by cracking the tubes and then soaking them in anhydrous ethanol for 2 h. Pure PAAm hydrogels were prepared in the same procedure without HNTs. The hydrogels synthesized by adding 0.4 g HNTs, 0.1 g, 0.2 g, and 0.4 g HNTs@HKUST-1 were noted as PAAm-HNTs, PAAm-HNTs@HKUST-1(0.5%), PAAm-HNTs@HKUST-1 (1%), and PAAm-HNTs@HKUST-1(2%), respectively. Percentages indicated the weight percentage of HNTs@HKUST-1 to water. The material formulation of the hydrogels is shown in Table S1.

2.4. Characterization

Aqueous suspensions (0.05 wt%) of the samples were dropped on the carbon support film to observe the microscopic morphology by transmission electron microscopy (TEM) (JEM-1400 Flash, JEOL Ltd., Japan) with an accelerating voltage of 120 kV. The surface morphology and section morphology of the samples were observed by scanning electron microscopy (SEM) (Zeiss Sigma 300). The hydrogel samples were lyophilized at −55 °C after being quenched in liquid nitrogen and

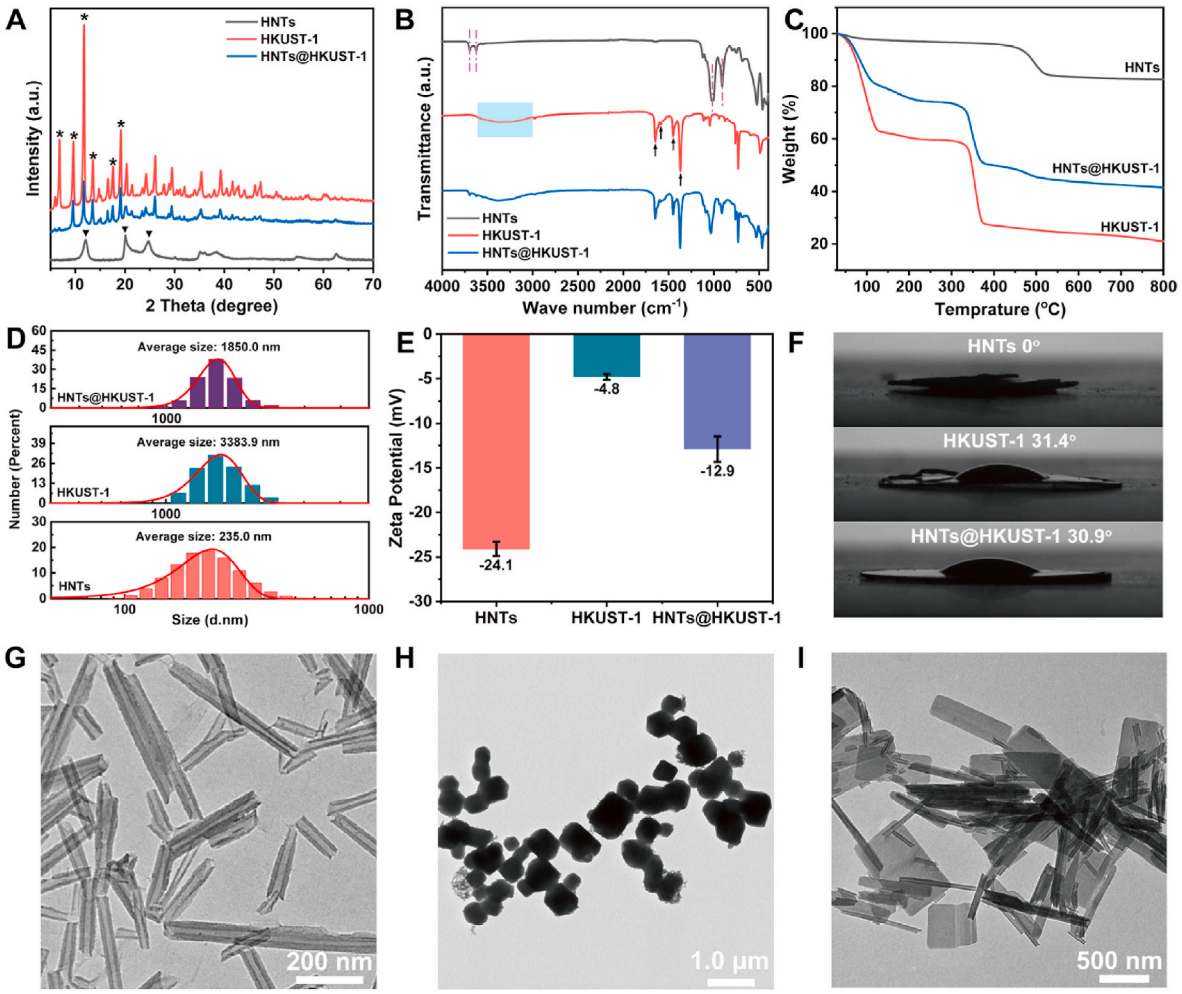

Fig. 2. Characterization of HNTs, HKUST-1, and HNTs@HKUST-1: (A) XRD patterns, (B) FTIR spectra, (C) Thermogravimetric curves, (D) Particle size distribution, (E) Zeta potential, (F) Static water contact angle. TEM images of (G) HNTs, (H) HKUST-1 and (I) HNTs@HKUST-1.

sprayed with a layer of gold before observation. N_2 adsorption and desorption of the sample powders were analyzed by a specific surface area and pore size analyzer (Quantachrome Instruments, America). Data of the nitrogen adsorption isotherm for pore analysis were processed according to NLDFT method to evaluate the pore size distribution and pore volume [31]. The crystal structure of the sample was obtained by X-ray diffraction instrument (XRD) (MiniFlex-600, Rigaku Corporation, Japan). The Fourier-transform infrared (FTIR) spectra were determined by FTIR instrument (UATR Two, PerkinElmer, USA). The thermal decomposition process of the sample was tested and analyzed using a thermogravimetric (TGA) machine (TGA2, METTLER TOLEDO Co. Ltd., Switzerland). The particle size distribution and surface potential of the samples were measured using a Nano-ZS instrument (Malvern Instruments Ltd., UK). The content of all elements in the sample was detected by X-ray photoelectron spectroscopy (XPS) (ESCALAB250Xi, Thermo Fisher Scientific Ltd., USA). The tensile properties of the hydrogels were tested by a universal testing machine (AGS-X, Shimadzu, Japan) at a rate of 50 mm/min.

2.5. Conductivity tests of PAAm-HNTs@HKUST-1 hydrogels

The resistance of the respective hydrogels was measured with a multimeter (Fluke 17B+) after removing them from the test tubes, and their conductivity was calculated by the following equation.

$$\text{Electrical conductivity} = \frac{L}{RS}$$

Where, L refers to the distance between the two ends of the multimeter probe during resistance measurement, R refers to the resistance measured and S refers to the cross-sectional area of the hydrogel.

2.6. Swelling rate and solvent loss rate tests of PAAm-HNTs@HKUST-1 hydrogels

A certain mass of hydrogel was immersed in water and weighed at specified intervals. The swelling rate was calculated based on the following equation.

$$\text{Swelling rate} = \frac{M - M_0}{M_0} \times 100\%$$

Where, M is the mass of the hydrogel after soaking for a specific time, and M_0 is the mass of the hydrogel before soaking.

Normal body temperature (37 °C) was difficult to control due to the limitation of experimental conditions, so a certain mass of hydrogel was put into the oven at 40 °C drying for 24 h, then the mass of the dry hydrogel (abbreviated as D-Hydrogel) was weighed. The solvent loss rate of the hydrogel was calculated according to the following equation.

$$\text{Solvent loss rate} = \frac{m_0 - m_t}{m_0} \times 100\%$$

Where, m_0 is the mass of the hydrogel before drying, and m_t is the mass of the D-Hydrogel after 24 h of drying in the oven.

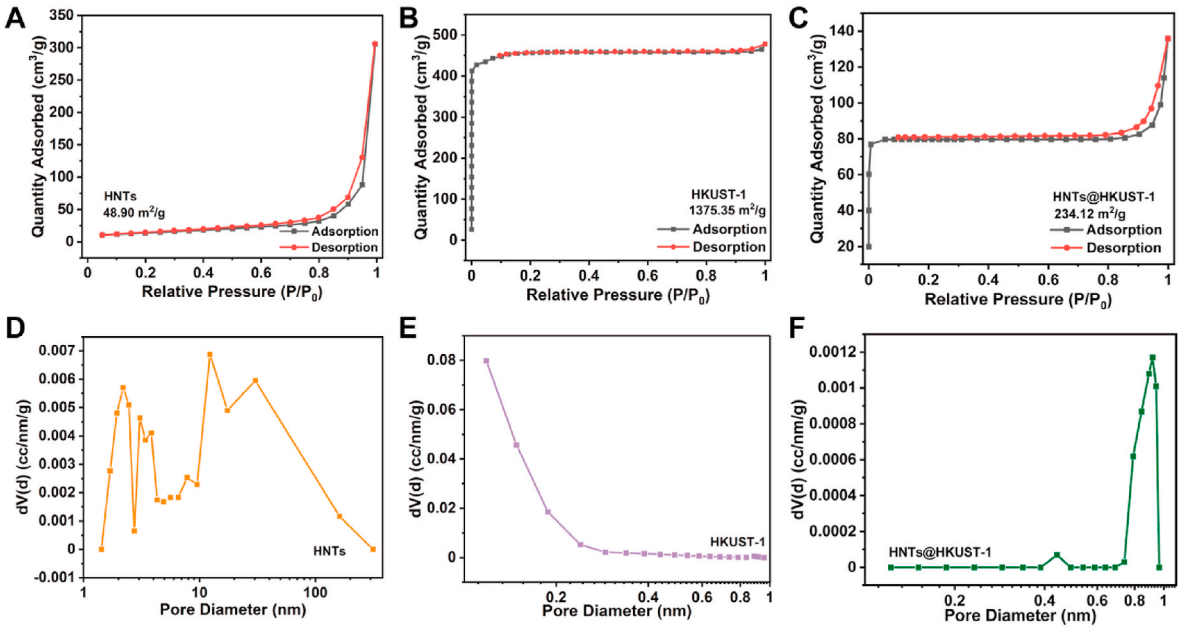

Fig. 3. Nitrogen adsorption-desorption isotherms and pore size distribution: (A, D) HNTs, (B, E) HKUST-1, (C, F) HNTs@HKUST-1.

2.7. In vitro antibacterial assays

The antibacterial property of HNTs@HKUST-1 was evaluated by the colony counting method. Gram-negative *Escherichia coli* (*E. coli*) and Gram-positive *Staphylococcus aureus* (*S. aureus*) were selected as the bacterial models. The bacteria were cultured with Luria-Bertani (LB) broth and incubated overnight at 37 °C in a constant temperature shaker at 150 rpm. The bacteria were diluted 10^4 times with LB broth, and the density of the bacteria after dilution was about 1×10^5 CFU/mL. After that, 10 mg HNTs, 2.5 mg, 5 mg, and 10 mg HNTs@HKUST-1 were respectively added to 5 mL of the diluted bacterial suspension. After incubation in a constant temperature shaker for 4 h, 100 μL of the mixture was aspirated from each group and dropped onto the LB agar. Then the mixture was spread evenly with a spreader until dry and placed in a 37 °C incubator for 12 h. The control group was diluted bacterial suspensions without any extra materials. The bacterial inhibition rate was obtained by counting the colonies formed on the agar plates and then calculated by the following equation.

$$\text{Bacterial inhibition rate} = \frac{C - C_a}{C} \times 100\%$$

Where, C is the number of colonies in the control group, and C_a is the number of colonies in each group after incubation.

The bacterial growth curve was determined by co-cultivating the diluted bacterial suspension with the material, then aspirating 100 μL of the solution at specific intervals, and measuring the absorbance value at 600 nm using a microplate reader.

2.8. Detection of human movement by PAAm-HNTs@HKUST-1 hydrogel

To monitor the body's movement, the hydrogels were cut into strips of appropriate length and taped to the corresponding joints of the body, such as the wrist, finger, knee, and elbow joints. A copper wire was used to connect the two ends of the hydrogel to the electrometer. Resistance changes were recorded with an electrometer (KEITHLEY 6514, Tektronix Technology Co., Ltd., China). The relative resistance change was calculated based on the following equation.

$$\text{Relative resistance} = \frac{R}{R_0}$$

Where, R is the resistance of the hydrogel after deformation and R_0 is the resistance of the hydrogel without deformation.

3. Results and discussion

3.1. Characterization of HNTs@HKUST-1 nanocomposites

HNTs can be used as supporters of many types of nanoparticles, such as metal, metal oxide, and carbon. The *in-situ* growth method was commonly used to synthesize these heterostructures, and the modification process brought multi-functional properties to HNTs. Based on our previous work on synthesizing HNTs@MOFs, this work developed a new hybrid material composed of HNTs and HKUST-1 in a water/ethanol system.

The XRD pattern of HNTs, HKUST-1, and HNTs@HKUST-1 were used to study their crystal structures (Fig. 2A). XRD pattern of HKUST-1 was in general agreement with that reported in the literature [30,32], indicating that HKUST-1 was successfully synthesized. The characteristic peaks can be clearly seen in the pattern of HKUST-1 at $2\theta = 6.8^o$, 9.6^o, 11.7^o, 13.6^o, 17.6^o, and 19.1^o. The characteristic peaks of HKUST-1 were also found in the XRD pattern of HNTs@HKUST-1, indicating the existence of HKUST-1 framework units in the composites. But, the peak around $2\theta = 6.8^o$, 27.8^o, and 34.0^o of HKUST-1 disappeared in the composites, suggesting some changes occurred in the crystal structure of the MOFs. HNTs have three characteristic peaks at 12.1^o, 20.1^o, and 24.7^o, assigned to (001), (020, 110), and (002) planes, but they were not evident in the pattern of HNTs@HKUST-1. The characteristic peaks of HNTs may be covered by the high-intensity peak of HKUST-1.

In the IR spectrum (Fig. 2B), the absorption peaks of HNTs at 3697 cm^{-1} and 3623 cm^{-1} were derived from the stretching vibration of –OH on the inner surface of HNTs [33], while the peaks at 1022 cm^{-1} and 911 cm^{-1} were respectively attributed to Si–O–Si and -Al-O. In the IR spectrum of HKUST-1, the broadband appearing at 2900-3700 cm^{-1} indicated the presence of water and –OH groups in its structure [32], and the peaks appearing at 1370, 1450 cm^{-1} and 1588, 1645 cm^{-1} corresponded to the symmetric and asymmetric stretching vibrations of the carboxylate group, respectively. The characteristic peaks of both HNTs and HKUST-1 were present in the IR spectrum of HNTs@HKUST-1, which proved that the two materials are successfully combined.

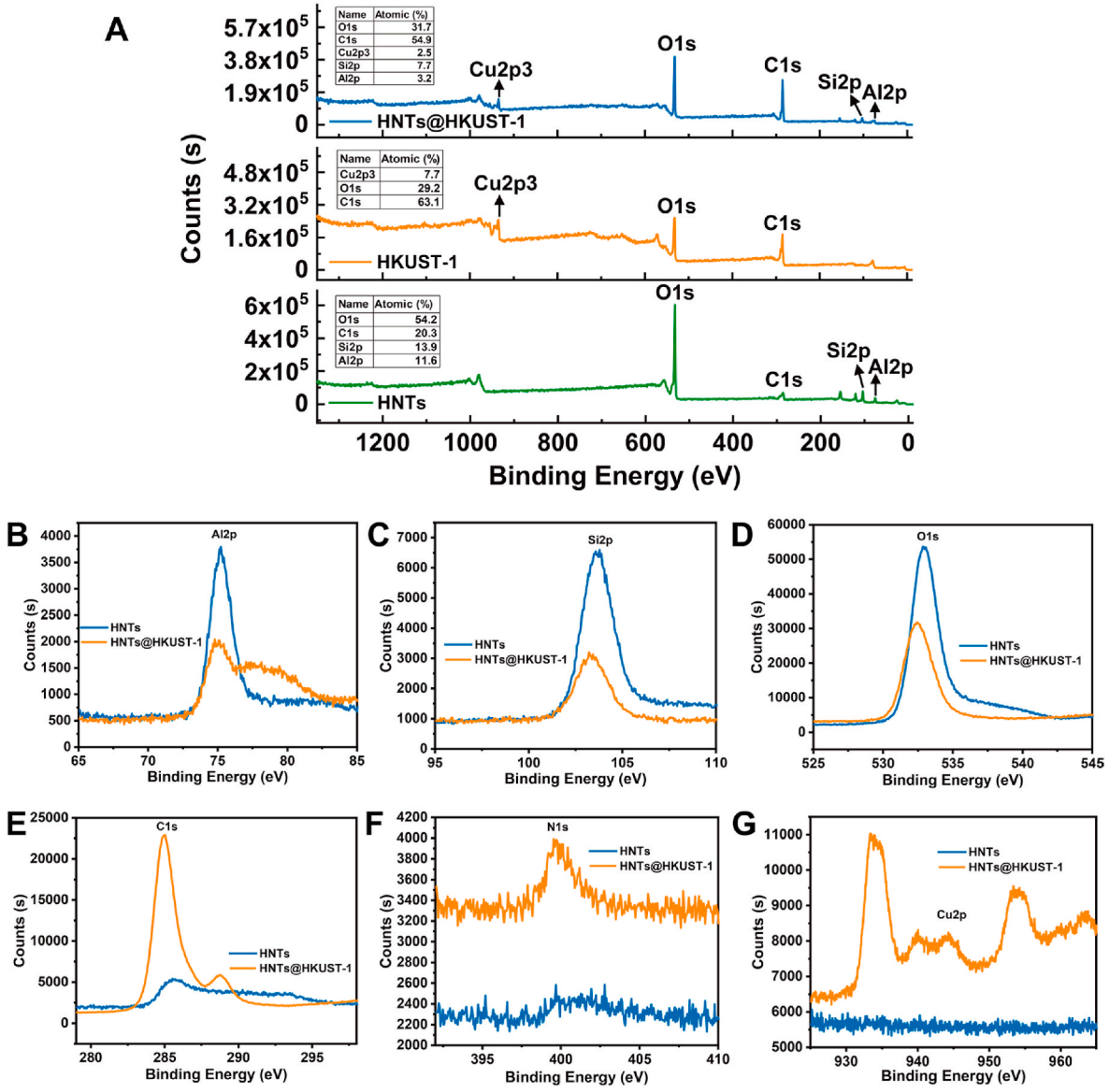

Fig. 4. (A) XPS survey scans of HNTs, HKUST-1, and HNTs@HKUST-1. (B–G) High-resolution XPS spectrum of Al, Si, O, C, N, and Cu elements.

The thermal decomposition process of the materials was then studied (Fig. 2C). HNTs have high-temperature resistance, and maximum thermal decomposition occurred at about 442.0 °C, while the slight mass loss that occurred at around 100.0 °C was caused by the evaporation of water. The mass loss of HKUST-1 before 327.5 °C was mainly due to the evaporation of the solvent remaining in the pores and the removal of unreacted guest molecules. As the temperature reached 800 °C, the remaining mass was only 21.0%. In addition, the structure of HNTs@HKUST-1 collapsed at 332.5 °C, and the mass reduced to 41.5% at 800 °C. The copper content in HNTs@HKUST-1 was calculated as 14.0% from the TG results. The particle size of the nanoparticles was studied as shown in Fig. 2D. The average sizes of HNTs, HKUST-1, and HNTs@HKUST-1 were 235.0 nm, 3383.9 nm, and 1850.0 nm, respectively. The increased size of HNTs suggested the combination of the clay and MOFs. In addition, to study the surface properties of these materials, the zeta potential of their aqueous solutions was tested. The results showed (Fig. 2E) that they were all negatively charged, and the zeta potential of HNTs, HKUST-1, and HNTs@HKUST-1 were −24.1, −4.8, and −12.9 mV, respectively. To investigate the hydrophilic properties of the material, the static water contact angle testing was performed, as shown in Fig. 2F. It demonstrated that no water droplets were formed on the surface of the HNTs tablet, indicating its extremely high hydrophilicity. The static water contact angles of HKUST-1 and HNTs@HKUST-1 were 31.4° and 30.9°, indicating that they were also hydrophilic materials, which helps them to disperse well in aqueous solutions.

The morphologies of HNTs, HKUST-1, and HNTs@HKUST-1 were observed by TEM. Fig. 2G exhibited the typical hollow tubular structure of HNTs, while Fig. 2H displayed the hexagonal-like shape of HKUST-1. As shown in Fig. 2I, the morphology of HKUST-1 in HNTs@HKUST-1 was transformed into a 2D sheet structure. Besides, the SEM images of HNTs, HKUST-1, and HNTs@HKUST-1 are shown in Figure S1, from which one can easily see that HNTs are rod-shaped (Figure S1A) and HKUST-1 shows a polyhedral morphology (Figure S1B). However, the morphology of HNTs@HKUST-1 is a combination of rods and sheets (Figure S1C), which is consistent with the results of TEM. We speculate that it is because the introduction of HNTs restricts the coordination of Cu^{2+} in HKUST-1 with the carboxyl group in trimesic acid, which affects the formation of 3D structure. Meanwhile, water and ethanol as solvents may also affect the morphology of HKUST-1. These factors eventually led to the transformation of HKUST-1 from 3D to 2D, forming HKUST-1 nanosheets [34].

The specific surface area and pore size distribution of HNTs, HKUST-

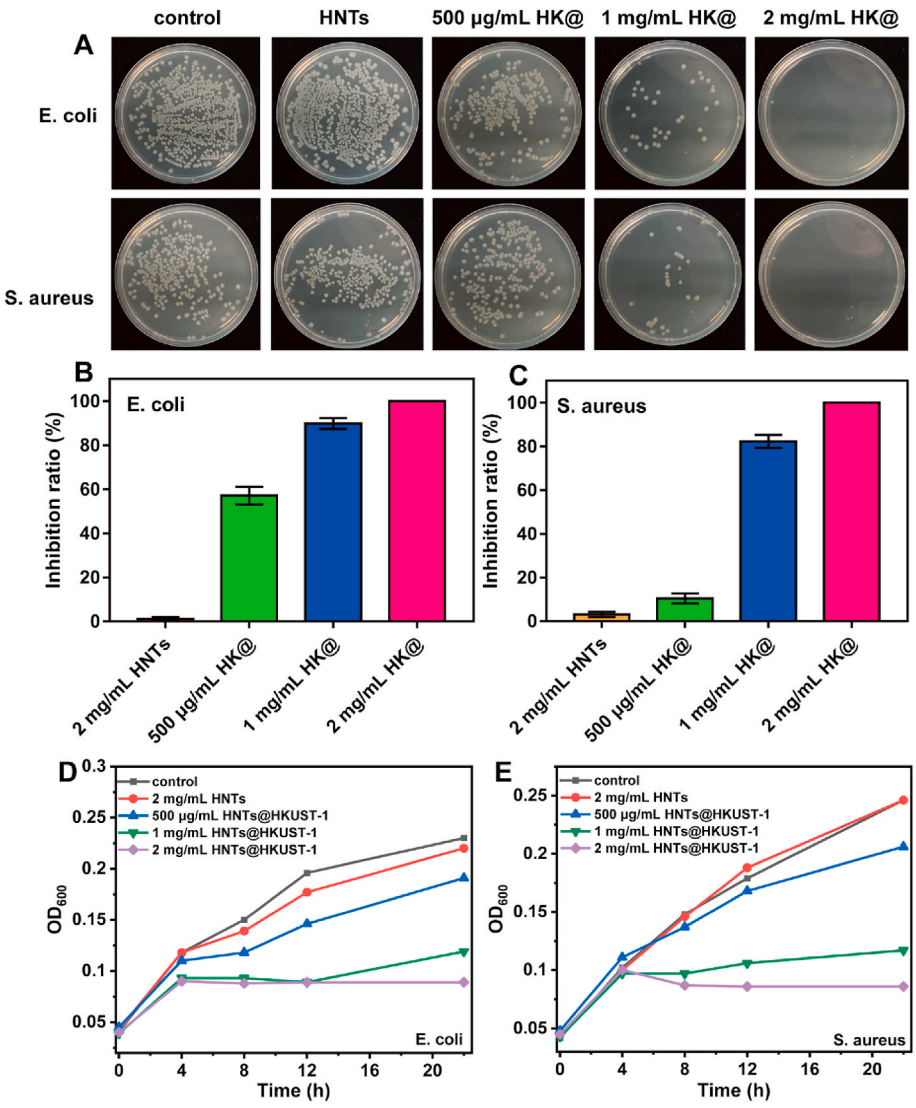

Fig. 5. (A) Comparison of *in vitro* antibacterial activity of HNTs and HNTs@HKUST-1. The kill ratios from colony count evaluation against *E. coli* (B) and *S. aureus* (C). Growth curves of *E. coli* (D) and *S. aureus* (E) in different groups. HNTs@HKUST-1 was abbreviated as HK@.

1, and HNTs@HKUST-1 were tested for comparison. As shown in Fig. 3A, the adsorption isotherm in the adsorption-desorption curve of HNTs was flat at low relative pressures. When the relative pressure was high, the adsorption isotherm rose rapidly, and the amount of adsorption and desorption of nitrogen were basically the same. This characteristic suggests that the adsorption-desorption isotherms of HNTs were consistent with type II adsorption behavior. The adsorption-desorption curves of HKUST-1 exhibited the type I isotherm characteristics of the microporous material, which was in agreement with the previous report [35] as shown in Fig. 3B. After testing the nitrogen adsorption-desorption curves (Fig. 3A–C), the specific surfaces area of HNTs, HKUST-1, and HNTs@HKUST-1 were 48.9, 1375.3, and 234.1 m^2/g, respectively. The pore size distribution of HNTs, HKUST-1, and HNTs@HKUST-1 was shown in Fig. 3D–F. Specifically, the pore size of HNTs was mainly in the range of 2.2–161.5 nm with both mesopores and macropores, while the pore sizes of both HKUST-1 and HNTs@HKUST-1 were below 1 nm, indicating that they were microporous materials.

To test the elemental composition on the surfaces of the materials, the XPS spectrum of HNTs, HKUST-1, and HNTs@HKUST-1 were detected. As shown in Fig. 4A, Cu, Si, and Al elements existed in HNTs@HKUST-1 with their contents of 2.5%, 7.7%, and 3.2%, respectively. Cu was derived from HKUST-1, while Al and Si were from HNTs, which proved that HKUST-1 and HNTs were successfully combined. Compared to pure HNTs, the Al, Si, and O contents in HNTs@HKUST-1 decreased from 11.6% to 3.2%, 13.9%–7.7%, and 54.2%–31.7%, respectively, while C content increased from 20.3% to 54.9%. It was demonstrated that the addition of HKUST-1 introduced Cu and increased C content, decreasing the proportion of Al, Si, and O content in HNTs. Also, the high-resolution XPS spectrum of Al, Si, O, C, N, and Cu elements of HNTs and HNTs@HKUST-1 were compared (Fig. 4B–G). In Fig. 4F, a small amount of N was found in HNTs@HKUST-1, which might be caused by impurities. In Fig. 4G, Cu 2p electrons existed in HNTs@HKUST-1, while it was not found in HNTs. Cu ions in the composite exhibited good antibacterial effect. Based on the TG results, the copper contents in PAAm-HNTs@HKUST-1(0.5%), PAAm-HNTs@HKUST-1(1%), and PAAm-HNTs@HKUST-1(2%) hydrogels can be calculated as 0.05 wt%, 0.10 wt%, and 0.21 wt%, respectively. The peaks of Al, Si, O, and C in HNTs@HKUST-1 shifted, indicating the chemical environment of these atoms changes due to the interactions between HKUST-1 and HNTs.

3.2. Antibacterial properties of HNTs@HKUST-1

The excellent antibacterial properties of HKUST-1 have been

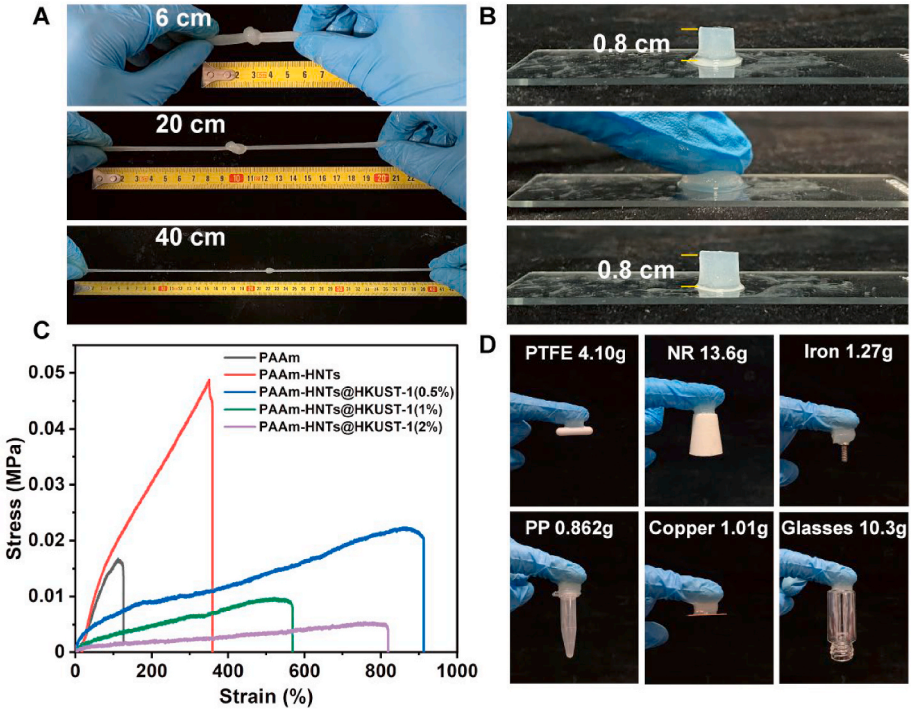

Fig. 6. Mechanical properties of PAAm-HNTs@HKUST-1 hydrogels: Appearances of the hydrogels were (A) stretched, and (B) compressed. (C) Stress-strain curves, (D) photographs of hydrogels adhered to different material surfaces (Polytetrafluoroethylene, PTFE; natural rubber, NR; polypropylene, PP).

extensively investigated. A possible explanation for its antibacterial mechanism is that the released Cu^{2+} is absorbed by bacteria and acts as an oxidizing agent for organic components, destroying the cell wall and leading to microbial death [36]. The bacterial assay was performed to verify whether the HNTs@HKUST-1 have antibacterial properties. *E. coli* (Gram-negative) and *S. aureus* (Gram-positive) were co-cultured with HNTs@HKUST-1 in LB broth for 4 h and then spread on agar plates to observe the number of colonies. As shown in Fig. 5A, the number of colonies of *E. coli* and *S. aureus* in the raw HNTs group and the control group were similar, showing no antibacterial properties of HNTs. The number of colonies of *E. coli* and *S. aureus* decreased rapidly with the increasing concentration of HNTs@HKUST-1, and when the concentration was 2 mg/mL, the bacteria on the agar plates had been completely killed. Fig. 5B and C showed the killing rate of *E. coli* and *S. aureus* corresponding to the colony counting method, respectively. The inhibition rates of HNTs@HKUST-1 at the concentrations of 500 μg/mL and 1 mg/mL were 57.2% and 89.9% for *E. coli* and 10.5% and 82.3% for *S. aureus*, respectively. So, it was evident that HNTs@HKUST-1 has a better inhibition effect towards *E. coli*. When the concentration of HNTs@HKUST-1 reached 2 mg/mL, the killing rate of both bacteria was 100%.

The antibacterial properties of HNTs@HKUST-1 were also investigated by testing the bacterial growth curves in a liquid broth medium. The growth of bacteria over time was monitored by detecting OD value at 600 nm [37]. The bacterial growth curves of *E. coli* and *S. aureus* incubated with different materials for 22 h were recorded as shown in Fig. 5. The control group was bacteria in a broth medium without any material. In Fig. 5D, the bacterial growth curves of the raw HNTs group showed similar growth trends and growth rates to those of the control group, indicating that HNTs do not have antibacterial properties. In the 500 μg/mL HNTs@HKUST-1 group, the growth of bacteria was slowed down after 4 h of incubation compared to the control group, indicating that Cu^{2+} played a critical role in inhibiting bacterial growth. When the concentration reached 2 mg/mL, the bacteria still grew in the first 4 h because the release of Cu^{2+} and the uptake of bacteria required a certain reaction time. After 4 h, the OD_{600} remained basically unchanged, indicating that the bacteria had been completely killed so that the antibacterial effect will last for a long time. Fig. 5E also demonstrated a similar trend. These results showed that HNTs@HKUST-1 had excellent antibacterial properties due to the release of Cu^{2+}, which provided a possibility for subsequent antibacterial applications in polymer composite hydrogels. Other copper-containing materials (e.g., copper oxides) also have antibacterial properties if they are added to hydrogel, which will be studied in the following studies.

3.3. Characterization of PAAm-HNTs@HKUST-1 composite hydrogels

The mechanical properties of the prepared PAAm-HNTs@HKUST-1 composite hydrogels were investigated. As shown in Fig. 6A, the hydrogel exhibited excellent extensibility, and the knotted hydrogel was slowly stretched from an initial length of 6 cm to almost 7 times its original length (40 cm) without breaking. Besides, when the hydrogel was compressed, it can return to its original shape, showing good self-recovery ability (Fig. 6B). To investigate the effect of HNTs@HKUST-1 on the mechanical properties of PAAm hydrogels, tensile tests of different hydrogels were performed. As shown in Fig. 6C, the elongations at break and tensile strength of the PAAm hydrogel were 126.4% and 16.8 kPa, respectively. The elongation at break and tensile strength of PAAm-HNTs hydrogels were increased to 359.3% and 48.8 kPa after adding HNTs as reinforcing agents. HNTs can act as a physical cross-linking agent for PAAm chains via hydrogen bonding, and the mechanical properties of PAAm-HNTs hydrogels were significantly enhanced because the cross-linking network of the hydrogels became tighter after immersion in ethanol [38]. Although the elongation at break of PAAm-HNTs hydrogel reached 359.3%, this was not sufficient to apply in human motion sensors to detect large motion movements, such as running, jumping, and so on. Therefore, the development of hydrogels with ultra-high strain was desired.

Different contents of HNTs@HKUST-1 were then introduced into PAAm hydrogels to balance the elongation at break and tensile strength of the hydrogels. In Fig. 6C, the tensile strength of the PAAm-HNTs@HKUST-1 hydrogels gradually decreased as the content of

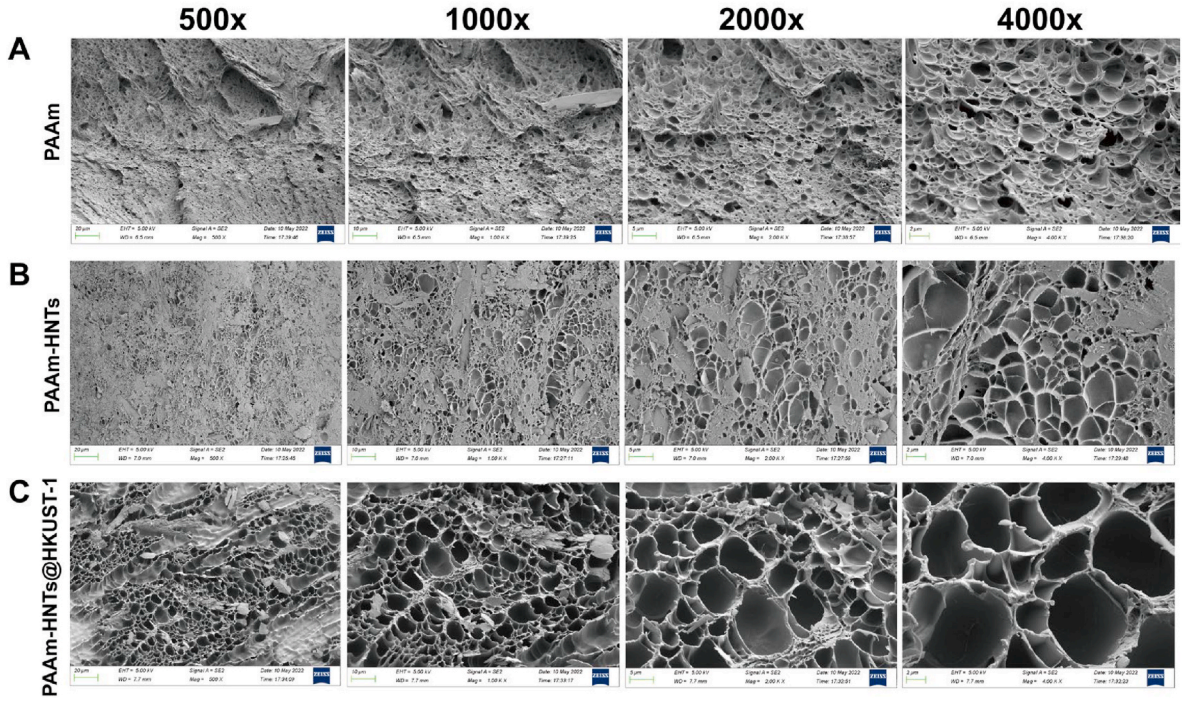

Fig. 7. SEM images of D-Hydrogel sections: (A) PAAm, (B) PAAm-HNTs, (C) PAAm-HNTs@HKUST-1(1%).

HNTs@HKUST-1 increased from 0.5% to 2%, but they exhibited a substantial elongation at break. When the content of HNTs@HKUST-1 was 0.5%, the elongation at break could reach 912.5%, and the tensile strength was 22.4 kPa. They changed to 569.3% and 9.5 kPa at 1%, 819.0% and 5.2 kPa at 2%. Obviously, the addition of HNTs@HKUST-1 caused the PAAm hydrogel to change from a hard and brittle to a soft and tough state. Although PAAm-HNTs@HKUST-1(0.5%) had the highest strain and tensile strength, the low content of HNTs@HKUST-1 was not beneficial to antibacterial property. PAAm-HNTs@HKUST-1 (2%) had lower tensile strength, and the material was too soft, which was unsuitable for practical application. Based on the comprehensive properties, PAAm-HNTs@HKUST-1(1%) was considered the candidate for the sensor application. The excellent adhesion of PAAm-HNTs@HKUST-1 hydrogel to different materials (plastic, rubber, and glass) was demonstrated in Fig. 6D. This high adhesion provided an opportunity for subsequent development of antimicrobial dressings in human.

The surface morphology of PAAm, PAAm-HNTs, and PAAm-HNTs@HKUST-1 D-Hydrogels was observed by SEM. As shown in Figure S2A, the PAAm D-Hydrogel exhibited a smooth surface, while the HNTs on the surface of the PAAm-HNTs D-Hydrogel can interact well with the matrix (Figure S2B), enhancing the mechanical properties of the hydrogel. Furthermore, the existence of HNTs was also found on the surface of PAAm-HNTs@HKUST-1 D-Hydrogel, as shown in Figure S2C. In addition, the cross-sections of PAAm, PAAm-HNTs, and PAAm-HNTs@HKUST-1 D-Hydrogels were observed by SEM, as shown in Fig. 7. All the D-Hydrogels exhibited porous structures. However, the pores of pure PAAm are mostly circular with smaller pore diameters (Fig. 7A). The cross-sections of PAAm-HNTs D-Hydrogels are mostly irregularly shaped pores with slightly larger pore diameters than those of pure PAAm (Fig. 7B). While the pores of the PAAm-HNTs@HKUST-1 D-Hydrogel cross-section became more regular in shape, and the pore

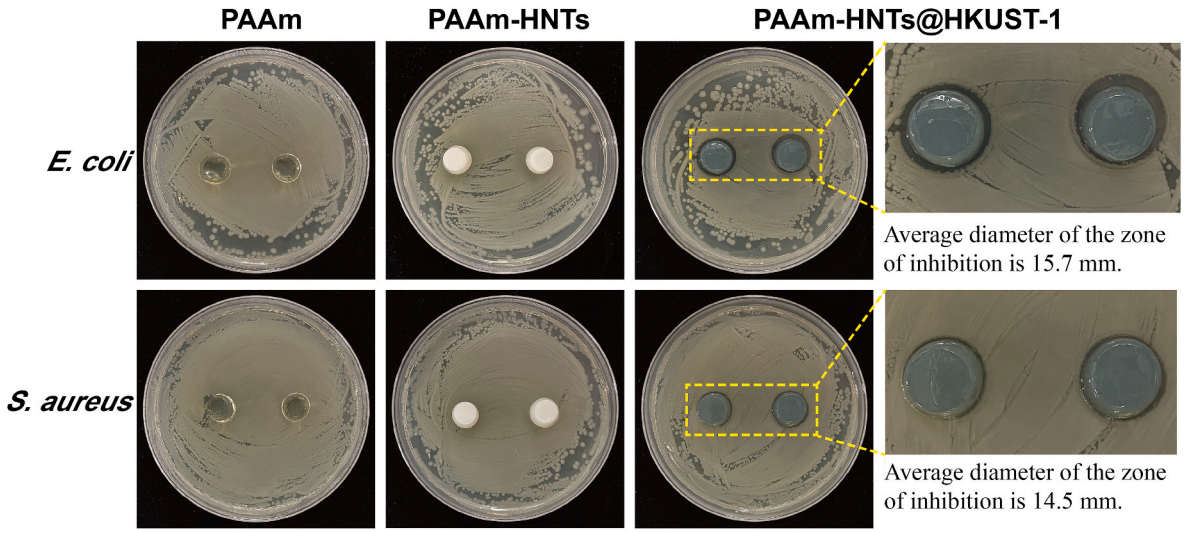

Fig. 8. The zone of inhibition results of PAAm, PAAm-HNTs, and PAAm-HNTs@HKUST-1 hydrogels (1%).

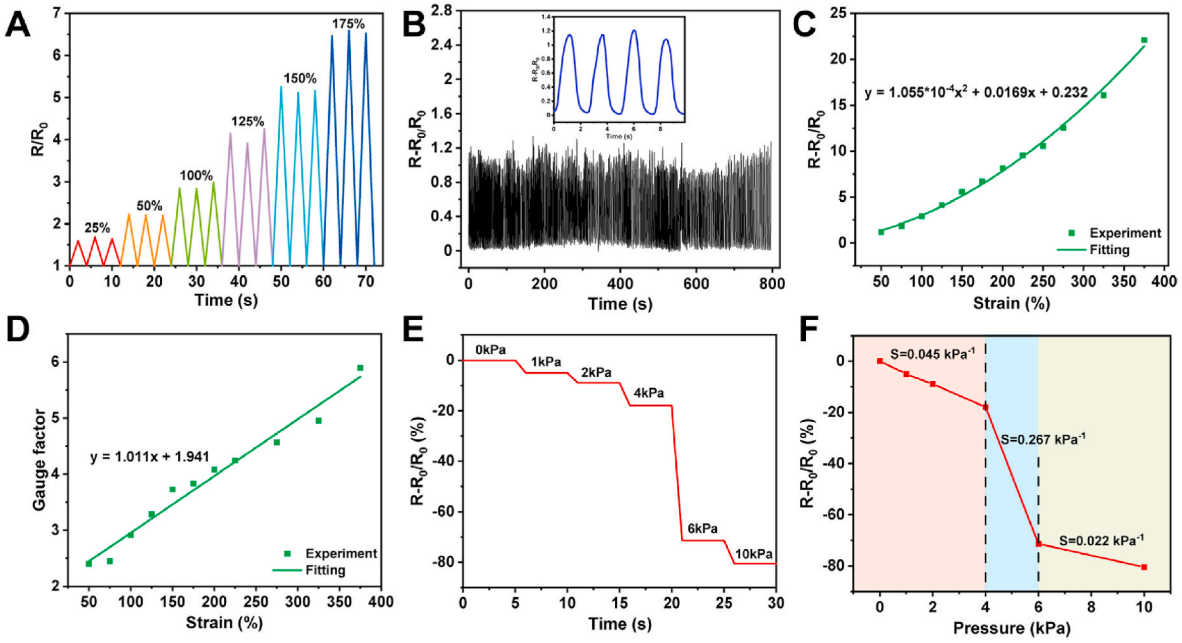

Fig. 9. Sensitivity of the PAAm-HNTs@HKUST-1 hydrogel-based sensor. (A) Changes in the relative resistance of the sensor with time at different tensile strains, (B) Relative resistance change under 400 cycles of stretching-releasing test at 50% tensile strain, (C) Relative resistance varies with increasing tensile strain, (D) The relationship between Gauge factor and tensile strain, (E) Relative resistance change with applied pressure, (F) Relative resistance change and pressure sensitivity at different pressures.

size was much larger than the other two D-Hydrogels (Fig. 7C).

The swelling of hydrogel is manifested by volume expansion and mass increase in response to water absorption [39]. The swelling rate of different hydrogels within 168 h was studied. As shown in Figure S3A, the swelling rate of PAAm-HNTs@HKUST-1 hydrogel was extremely large compared with PAAm and PAAm-HNTs, which showed the swelling rate of the hydrogel became larger with the addition of HNTs@HKUST-1. The reason for the larger swelling rate is related to the increased water molecule interactions and pore size of the composite hydrogels, as illustrated in Fig. 7. In addition, the swelling rate of PAAm-HNTs@HKUST-1 hydrogel was decreased after 120 h. This phenomenon is caused by the difficulty of completely collecting hydrogels for measurement because they fracture in water after swelling. The water content of a hydrogel can affect its comprehensive properties. For example, water loss can lead to loss of elasticity, reduced electrical conductivity, and deformation [40]. As shown in Figure S3B, the PAAm-based hydrogels maintained high water content after drying at 40 °C for 24 h. The solvent loss rates of the hydrogels were below 65%, except for PAAm-HNTs@HKUST-1 (2%), which exhibited a water loss rate of 68.2%.

The zone of inhibition (ZOI) was measured to verify the antibacterial properties of PAAm-HNTs@HKUST-1 hydrogel. As shown in Fig. 8, *S. aureus* and *E. coli* grew well in the PAAm and PAAm-HNTs groups, and no ZOI appeared around the hydrogels, indicating that the PAAm hydrogels and PAAm-HNTs hydrogels had no antibacterial activity against these two bacteria. However, a distinct ZOI was observed in the PAAm-HNTs@HKUST-1 group, which indicated no bacterial growth around the hydrogel on the Petri dishes. The results demonstrated that the PAAm-HNTs@HKUST-1 hydrogel had good antibacterial properties against both *S. aureus* and *E. coli*. In addition, the average diameter of the zone of inhibition was 15.7 mm for *E. coli* and 14.5 mm for *S. aureus*, indicating that PAAm-HNTs@HKUST-1 hydrogels exhibited better inhibition of *E. coli* compared to *S. aureus*, which suggests that PAAm-HNTs@HKUST-1 hydrogels have a stronger ability to kill Gram-negative bacteria.

3.4. Sensing performance of PAAm-HNTs@HKUST-1 composite hydrogel

The composite hydrogel exhibited high electrical conductivity due to HKUST-1. The conductivity of PAAm-HNTs@HKUST-1 (1%) was determined as 0.22 S/m, while the conductivity of PAAm was only 0.09 S/m. So, the improvement in the conductivity of the hydrogel is due to HKUST-1 although its poor electrical conductivity (Conductivity $<3 \times 10^{-9}$ S/m) [41]. The conductivity of the hydrogel was also attributed to the presence of the potassium ion in the hydrogel network originating from initiator potassium persulfate [38]. The resistance of PAAm-HNTs@HKUST-1 composite hydrogel changes with strain, so the composite hydrogel can be used as a strain sensor. The sensitivity and reliability were tested under tensile and compressive deformation, as shown in Fig. 9. Fig. 9A showed the change in relative resistance of PAAm-HNTs@HKUST-1 composite hydrogel sensor under cyclic stretch and released at 25%–175% strain. The relative resistance increased with strain, and it could be found that the relative resistance R/R_0 remained essentially the same for each stretch-release cycle at a certain strain. It showed that the strain sensor had excellent stability and flexibility. Furthermore, the durability and stability of the PAAm-HNTs@HKUST-1 composite hydrogel strain sensor were verified. As shown in Fig. 9B, it maintained a stable signal output after 400 stretching cycles, which indicated that the sensor was reliable. Meanwhile, the relative resistance change under the stretching cycles was not so stable, and the reasons included the evaporation of water or instrumentation errors during stretching, and the changes in the microstructure of the hydrogel during the stretching cycle, which resulted in stress relaxation [42].

Subsequently, the relationship between the relative resistance of the sensor calculated by $\Delta R/R_0$ and the strain was investigated, and it was found that they conformed to a quadratic functional relationship after fitting, as shown in Fig. 9C. The gauge factor (GF), defined as the ratio of the relative resistance to the strain, is a parameter used to evaluate the sensitivity of the strain sensors. As shown in Fig. 9D, the GF was linearly related to the strain, and a high GF indicated that the strain sensor was sensitive within the tested strain [40]. In addition, the GF value of the composite hydrogel reached up to 5.89 at 375% strain, which is comparable with those of recently reported strain sensors, such as the

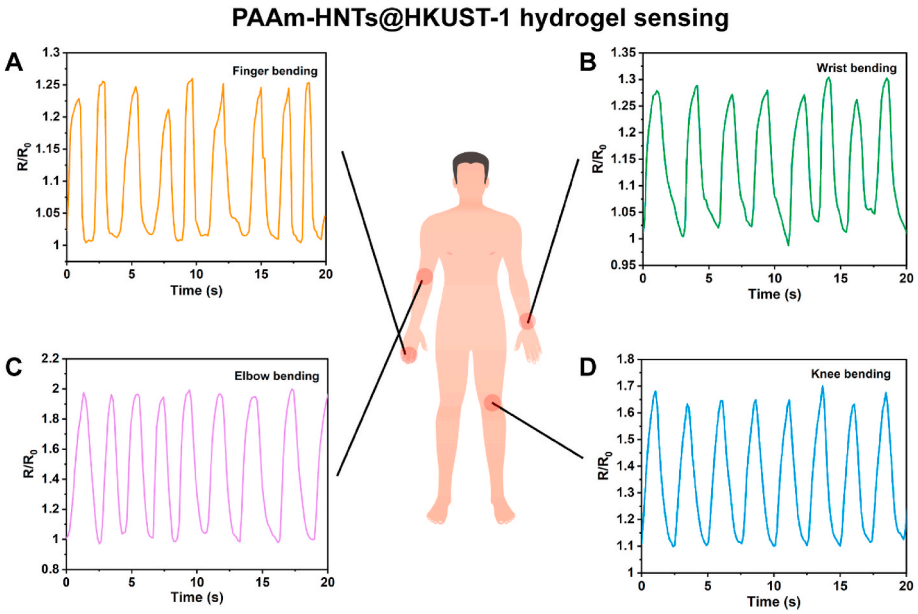

Fig. 10. Real-time monitoring of relative resistance changes for various human movements by PAAm-HNTs@HKUST-1 hydrogel. (A) Finger bending, (B) Wrist bending, (C) Elbow bending, and (D) Knee bending.

TEMPO-oxidized cellulose nanofibers (TOCNFs)-graphene nanocomposites reinforced polyacrylic acid (PAA) composite hydrogels (GF = 5.8 at 350% strain). While TOCNFs-carbon nanotubes nanocomposites reinforced PAA hydrogel showed GF of 6.86 at 400% strain, and TOCNF/polyaniline/PAA hybrid hydrogels exhibited GF of about 8 at strains above 300% [43–45]. Nevertheless, the detection limits of hydrogel-based sensors should be further optimized for practical applications.

The excellent elasticity of PAAm-HNTs@HKUST-1 hydrogel also allowed it to be used in pressure sensors. The resistance of the hydrogel decreased when the applied pressure increased, which showed the opposite trend to the tensile model due to the shorter ion transport channels, as shown in Fig. 9E. When the pressure was increased from 4 kPa to 6 kPa, the deformation of the hydrogel was the greatest, and the reduction in resistance was the most. Pressure sensitivity (S) referred to the slope of the relative resistance $\Delta R/R_0$ versus the pressure change curve, which represented the rate of variation of relative resistance to pressure. In Fig. 9F, the pressure sensitivity was divided into three regions, including a sensitivity of 0.045 kPa^{-1} at a pressure below 4 kPa, a sensitivity rising to 0.267 kPa^{-1} at a pressure of 4–6 kPa, and a sensitivity falling to 0.022 kPa^{-1} at a pressure of 6–10 kPa.

The high strain sensitivity, reusability, and ultra-high strain of PAAm-HNTs@HKUST-1 hydrogels showed the potential for application in human motion sensors. The hydrogel was then fixed at the fingers, wrists, elbows, and knees of a volunteer and connected to an electrometer with a wire, and the change in resistance with body movement was recorded. The hydrogel adheres to the body very well and does not peel off easily during this process. When the hydrogel deformed with the bending and stretching of the joint, the resistance of the PAAm-HNTs@HKUST-1 hydrogel sensor also made simultaneous changes. The finger bending action could be detected as displayed in Fig. 10A. It can clearly demonstrate that the R/R_0 value of the hydrogel increased rapidly with the bending of the finger, but when the finger was straightened, the value returned to its original state. Upon repeatedly bending and straightening the finger, the peak of relative resistance also changed regularly in real time, which could produce a stable sensing signal. In addition, the conductive hydrogel can also detect signals from large movements of the wrist (Fig. 10B), the elbow (Fig. 10C), and the knee (Fig. 10D). The sensing data detected from different limb sites showed that the signals were consistent and reproducible. These results suggested that PAAm-HNTs@HKUST-1 hydrogels showed great potential for application in the field of precise detection of human motion.

4. Conclusion

Sheet-like HKUST-1 was synthesized through a water/ethanol system by incorporating HNTs. HNTs depressed the crystal growth of the HKUST-1, which led to a 2D nanosheet morphology of this MOF. The Cu^{2+} in HKUST-1 endows excellent antibacterial properties on the composite. HNTs@HKUST-1 was used as a reinforcement for polyacrylamide (PAAm) hydrogels, and the PAAm-HNTs@HKUST-1 hydrogels have high tensile strain properties (elongation at break of 912.5% and tensile strength of 22.4 kPa). The presence of Cu^{2+} makes the composite hydrogels have remarkable electrical conductivity and antibacterial properties. The composite hydrogel was then developed as a strain sensor and human motion detection with high sensitivity, which has the advantages of antibacterial property, repeatability, and fast responsive ability. The prepared high-strength composite hydrogels have great potential as flexible and antibacterial materials to monitor the movements of the human body in real time.

CRediT authorship contribution statement

Wanli Zhao: Writing – original draft, Investigation. **Yuanhui Long:** Writing – original draft, Investigation. **Yunqing He:** Validation, Methodology. **Jiabing Cai:** Software, Methodology. **Mingxian Liu:** Writing – review & editing, Supervision, Funding acquisition.

Declaration of competing interest

The authors declare that they have no known competing financial interests or personal relationships that could have appeared to influence the work reported in this paper.

Data availability

No data was used for the research described in the article.

Acknowledgements

This work was financially supported by the National Natural Science Foundation of China (52073121), the Natural Science Foundation of Guangdong Province (2019A1515011509), the Science and Technology Program of Guangzhou (202102010117), and the Fundamental Research Funds for the Central Universities (21622406).

Appendix A. Supplementary data

Supplementary data related to this article can be found at https://doi.org/10.1016/j.micromeso.2022.112207.

References

[1] H. Park, Y.R. Jeong, J. Yun, S.Y. Hong, S. Jin, S.-J. Lee, et al., Stretchable array of highly sensitive pressure sensors consisting of polyaniline nanofibers and Au-coated polydimethylsiloxane micropillars, ACS Nano 9 (10) (2015) 9974–9985.
[2] T. Zhu, Y. Cheng, C. Cao, J. Mao, L. Li, J. Huang, et al., A semi-interpenetrating network ionic hydrogel for strain sensing with high sensitivity, large strain range, and stable cycle performance, Chem. Eng. J. 385 (2020), 123912.
[3] Y. Peng, M. Pi, X. Zhang, B. Yan, Y. Li, L. Shi, et al., High strength, antifreeze, and moisturizing conductive hydrogel for human-motion detection, Polymer 196 (2020), 122469.
[4] D. Zhao, Y. Zhu, W. Cheng, W. Chen, Y. Wu, H. Yu, Cellulose-based flexible functional materials for emerging intelligent electronics, Adv. Mater. 33 (28) (2021), 2000619.
[5] H. Zhang, J. Guo, Y. Wang, L. Sun, Y. Zhao, Stretchable and conductive composite structural color hydrogel films as bionic electronic skins, Adv. Sci. 8 (20) (2021), 2102156.
[6] M. Liao, P. Wan, J. Wen, M. Gong, X. Wu, Y. Wang, et al., Wearable, healable, and adhesive epidermal sensors assembled from mussel-inspired conductive hybrid hydrogel framework, Adv. Funct. Mater. 27 (48) (2017), 1703852.
[7] G. Ge, W. Yuan, W. Zhao, Y. Lu, Y. Zhang, W. Wang, et al., Highly stretchable and autonomously healable epidermal sensor based on multi-functional hydrogel frameworks, J. Mater. Chem. 7 (11) (2019) 5949–5956.
[8] Y. Liu, K. He, G. Chen, W.R. Leow, X. Chen, Nature-inspired structural materials for flexible electronic devices, Chem. Rev. 117 (20) (2017) 12893–12941.
[9] S.A. Khan, L.A. Shah, M. Shah, I. Jamil, Engineering of 3D polymer network hydrogels for biomedical applications: a review, Polym. Bull. (2021) 1–21.
[10] Y. Zhang, X. Tian, Q. Zhang, H. Xie, B. Wang, Y. Feng, Hydrochar-embedded carboxymethyl cellulose-g-poly (acrylic acid) hydrogel as stable soil water retention and nutrient release agent for plant growth, J. Bioresour. Bioprod. 7 (2) (2022) 116–127.
[11] A. Madni, R. Kousar, N. Naeem, F. Wahid, Recent advancements in applications of chitosan-based biomaterials for skin tissue engineering, J. Bioresour. Bioprod. 6 (1) (2021) 11–25.
[12] Z. Chen, Y. Chen, M.S. Hedenqvist, C. Chen, C. Cai, H. Li, et al., Multifunctional conductive hydrogels and their applications as smart wearable devices, J. Mater. Chem. B 9 (11) (2021) 2561–2583.
[13] Q. Rong, W. Lei, M. Liu, Conductive hydrogels as smart materials for flexible electronic devices, Chem. Eur J. 24 (64) (2018) 16930–16943.
[14] X. Liu, Y. Ma, X. Zhang, J. Huang, Cellulose nanocrystal reinforced conductive nanocomposite hydrogel with fast self-healing and self-adhesive properties for human motion sensing, Colloids Surf. A Physicochem. Eng. Asp. 613 (2021), 126076.
[15] Y. Wei, L. Xiang, H. Ou, F. Li, Y. Zhang, Y. Qian, et al., MXene-based conductive organohydrogels with long-term environmental stability and multifunctionality, Adv. Funct. Mater. 30 (48) (2020), 2005135.
[16] X. Sun, Z. Qin, L. Ye, H. Zhang, Q. Yu, X. Wu, et al., Carbon nanotubes reinforced hydrogel as flexible strain sensor with high stretchability and mechanically toughness, Chem. Eng. J. 382 (2020), 122832.
[17] F.-L. Yi, F.-C. Meng, Y.-Q. Li, P. Huang, N. Hu, K. Liao, et al., Highly stretchable CNT Fiber/PAAm hydrogel composite simultaneously serving as strain sensor and supercapacitor, Compos. B Eng. 198 (2020), 108246.
[18] Y. Yu, F. Xie, X. Gao, L. Zheng, Double-network hydrogels with adjustable surface morphology and multifunctional integration for flexible strain sensors, Soft Matter 17 (16) (2021) 4352–4362.
[19] J. Wang, L. Lin, Q. Cheng, L. Jiang, A strong bio-inspired layered PNIPAM–clay nanocomposite hydrogel, Angew. Chem. Int. Ed. 51 (19) (2012) 4676–4680.
[20] X. You, H. Wu, R. Zhang, Y. Su, L. Cao, Q. Yu, et al., Metal-coordinated sub-10 nm membranes for water purification, Nat. Commun. 10 (1) (2019) 1–10.
[21] Y. Xiang, G. Zhang, C. Chen, B. Liu, D. Cai, Z. Wu, Fabrication of a pH-responsively controlled-release pesticide using an attapulgite-based hydrogel, ACS Sustain. Chem. Eng. 6 (1) (2018) 1192–1201.
[22] C. Cheng, Y. Gao, W. Song, Q. Zhao, H. Zhang, H. Zhang, Halloysite nanotube-based H_2O_2-responsive drug delivery system with a turn on effect on fluorescence for real-time monitoring, Chem. Eng. J. 380 (2020), 122474.
[23] Y. Lvov, A. Panchal, Y. Fu, R. Fakhrullin, M. Kryuchkova, S. Batasheva, et al., Interfacial self-assembly in halloysite nanotube composites, Langmuir 35 (26) (2019) 8646–8657.
[24] X. Zhao, C. Zhou, M. Liu, Self-assembled structures of halloysite nanotubes: towards the development of high-performance biomedical materials, J. Mater. Chem. B 8 (5) (2020) 838–851.
[25] A.C. Santos, C. Ferreira, F. Veiga, A.J. Ribeiro, A. Panchal, Y. Lvov, et al., Halloysite clay nanotubes for life sciences applications: from drug encapsulation to bioscaffold, Adv. Colloid Interface Sci. 257 (2018) 58–70.
[26] G. Cavallaro, G. Lazzara, S. Milioto, F. Parisi, V. Evtugyn, E. Rozhina, et al., Nanohydrogel formation within the halloysite lumen for triggered and sustained release, ACS Appl. Mater. Interfaces 10 (9) (2018) 8265–8273.
[27] M. Massaro, G. Buscemi, L. Arista, G. Biddeci, G. Cavallaro, F. D'Anna, et al., Multifunctional carrier based on halloysite/laponite hybrid hydrogel for kartogenin delivery, ACS Med. Chem. Lett. 10 (4) (2018) 419–424.
[28] Z. Jia, T. Xu, S. Yang, Y. Luo, D. Jia, Interfacial mechano-chemical grafting in styrene-butadiene rubber/halloysite nanotubes composites, Polym. Test. 54 (2016) 29–39.
[29] P. Thoniyot, M.J. Tan, A.A. Karim, D.J. Young, X.J. Loh, Nanoparticle–hydrogel composites: concept, design, and applications of these promising, multi-functional materials, Adv. Sci. 2 (1–2) (2015), 1400010.
[30] C-S J, C-A V, Bn HI, T-C A, IA I, R-I JE, et al., Synthesis and characterization of an SWCNT@ HKUST-1 composite: enhancing the CO_2 adsorption properties of HKUST-1, ACS Omega 4 (3) (2019) 5275–5282.
[31] G. Kupgan, T.P. Liyana-Arachchi, C.M. Colina, NLDFT pore size distribution in amorphous microporous materials, Langmuir 33 (42) (2017) 11138–11145.
[32] S. Salehi, M. Anbia, High CO_2 adsorption capacity and CO_2/CH_4 selectivity by nanocomposites of MOF-199, Energy Fuel. 31 (5) (2017) 5376–5384.
[33] M. Wang, J. Wang, W. Hu, Preparation and corrosion behavior of Cu-8-HQ@ HNTs/epoxy coating, Prog. Org. Coating 139 (2020), 105434.
[34] G. Zhan, H.C. Zeng, Synthesis and functionalization of oriented metal–organic-framework nanosheets: toward a series of 2D catalysts, Adv. Funct. Mater. 26 (19) (2016) 3268–3281.
[35] V. Chevalier, J. Martin, D. Peralta, A. Roussey, F. Tardif, Performance of HKUST-1 Metal-Organic Framework for a VOCs mixture adsorption at realistic concentrations ranging from 0.5 to 2.5 ppmv under different humidity conditions, J. Environ. Chem. Eng. 7 (3) (2019), 103131.
[36] S. Shams, W. Ahmad, A.H. Memon, S. Shams, Y. Wei, Q. Yuan, et al., Cu/H_3BTC MOF as a potential antibacterial therapeutic agent against Staphylococcus aureus and Escherichia coli, New J. Chem. 44 (41) (2020) 17671–17678.
[37] Y. Wu, Y. Yang, Z. Zhang, Z. Wang, Y. Zhao, L. Sun, A facile method to prepare size-tunable silver nanoparticles and its antibacterial mechanism, Adv. Powder Technol. 29 (2) (2018) 407–415.
[38] K. Feng, G.-Y. Hung, X. Yang, M. Liu, High-strength and physical cross-linked nanocomposite hydrogel with clay nanotubes for strain sensor and dye adsorption application, Compos. Sci. Technol. 181 (2019), 107701.
[39] H. Lei, J. Zhao, X. Ma, H. Li, D. Fan, Antibacterial dual network hydrogels for sensing and human health monitoring, Adv Healthc Mater 10 (21) (2021), 2101089.
[40] Y. Ye, Y. Zhang, Y. Chen, X. Han, F. Jiang, Cellulose nanofibrils enhanced, strong, stretchable, freezing-tolerant ionic conductive organohydrogel for multi-functional sensors, Adv. Funct. Mater. 30 (35) (2020), 2003430.
[41] M. Alfè, V. Gargiulo, L. Lisi, R. Di Capua, Synthesis and characterization of conductive copper-based metal-organic framework/graphene-like composites, Mater. Chem. Phys. 147 (3) (2014) 744–750.
[42] Y.-Q. Li, P. Huang, W.-B. Zhu, S.-Y. Fu, N. Hu, KJSr Liao, Flexible wire-shaped strain sensor from cotton thread for human health and motion detection, Sci. Rep. 7 (1) (2017) 1–7.
[43] C. Zheng, K. Lu, Y. Lu, S. Zhu, Y. Yue, X. Xu, et al., A stretchable, self-healing conductive hydrogels based on nanocellulose supported graphene towards wearable monitoring of human motion, Carbohydr. Polym. 250 (2020), 116905.
[44] Y. Jiao, K. Lu, Y. Lu, Y. Yue, X. Xu, H. Xiao, et al., Highly viscoelastic, stretchable, conductive, and self-healing strain sensors based on cellulose nanofiber-reinforced polyacrylic acid hydrogel, Cellulose 28 (7) (2021) 4295–4311.
[45] Y. Jiao, Y. Lu, K. Lu, Y. Yue, X. Xu, H. Xiao, et al., Highly stretchable and self-healing cellulose nanofiber-mediated conductive hydrogel towards strain sensing application, J. Colloid Interface Sci. 597 (2021) 171–181.

Supporting Information

HNTs@HKUST-1 strengthened PAAm hydrogel for strain sensing and antibacterial application

Wanli Zhao, Yuanhui Long, Yunqing He, Jiabing Cai, Mingxian Liu*

Department of Materials Science and Engineering, College of Chemistry and Materials Science, Jinan University, Guangzhou 511443, People's Republic of China.

Email: liumx@jnu.edu.cn

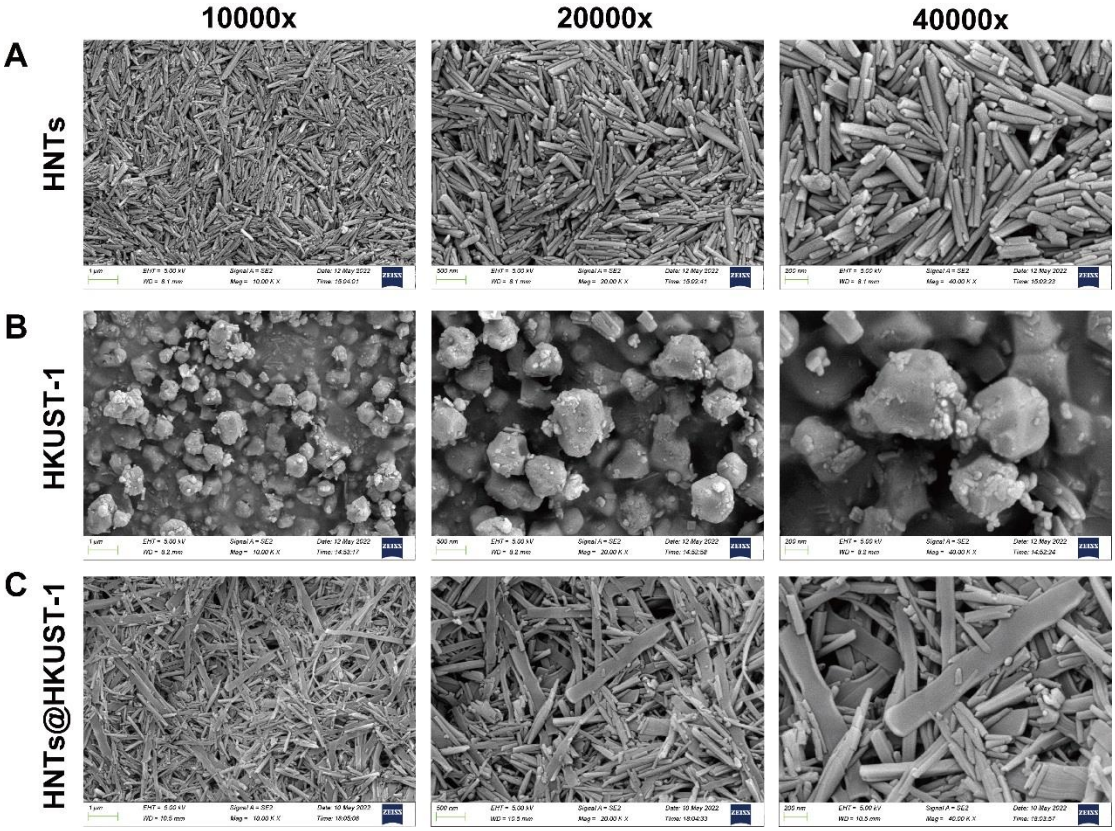

Figure S1. SEM images of (A) HNTs, (B) HKUST-1 and (C) HNTs@HKUST-1.

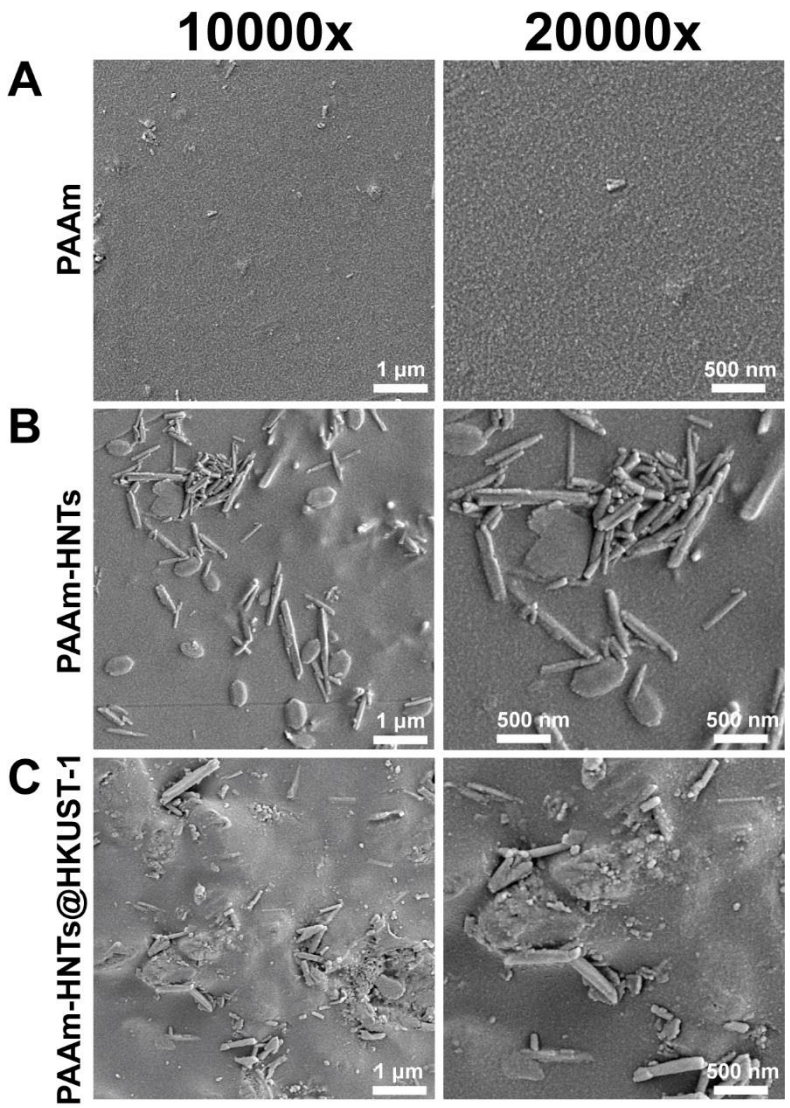

Figure S2. SEM images of hydrogel surfaces: (A) PAAm, (B) PAAm-HNTs, (C) PAAm-HNTs@HKUST-1.

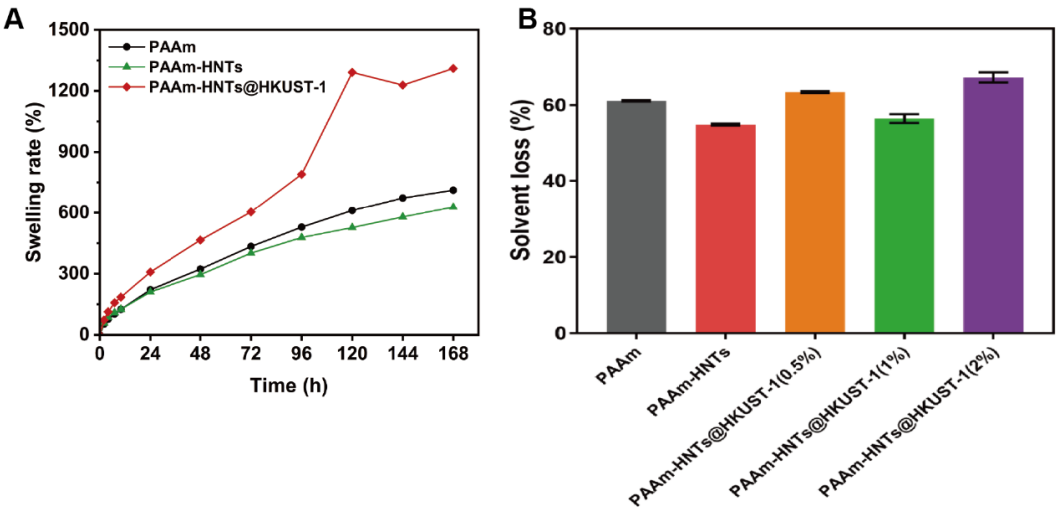

Figure S3. (A) Swelling rate curve with time (168 h) and (B) solvent loss rate of different hydrogels at 24 h.

Table S1 Chemical composition for preparation of the hydrogels.

Samples	AM (g)	H_2O (mL)	KPS (g)	HNTs (g)	HKUST-1@HNTs (g)
PAAm	3	23	0.6	0	0
PAAm-HNTs	3	23	0.6	4	0
PAAm-HNTs@HKUST-1(0.5%)	3	23	0.6	0	1
PAAm-HNTs@HKUST-1(1%)	3	23	0.6	0	2
PAAm-HNTs@HKUST-1(2%)	3	23	0.6	0	4